Nucleic Acids Research, 2026, **54**, gkag362
https://doi.org/10.1093/nar/gkag362
Chemical Biology and Nucleic Acid Chemistry

In situ tracking of glycoRNAs on single-cell surface to reveal RNA heterogeneity and transport mechanism

Meilin Gong[1,†], Xiaoqi Tang[2,†], Zuowei Xie[1], Ben Niu[1], Ruijia Deng[1], Wenjuan Fu[1], Yingjie Yang[1], Yu Tang[1], Jie Luo[1], Jing Sheng[1], Ying Zhang[3,*], Ming Chen[1,*], Kai Chang[1,*]

[1]Department of Clinical Laboratory Medicine, Southwest Hospital, Third Military Medical University (Army Medical University), 30 Gaotanyan, Shapingba District, Chongqing 400038, China
[2]Department of Laboratory Medicine, The First Medical Center of Chinese PLA General Hospital, Beijing 100853, China
[3]Deputy Director and Associate Professor of the Joint Surgery Center at Southwest Hospital, Third Military Medical University, 30 Gaotanyan, Shapingba, Chongqing 400038, China

*To whom correspondence should be addressed. Email: changkai0203@tmmu.edu.cn
Correspondence may also be addressed to Ming Chen. Email: chming1971@126.com
Correspondence may also be addressed to Ying Zhang. Email: zhang.ying@live.cn
†These authors contributed equally.

Abstract

Cell-surface glycoRNA plays a crucial role in cellular behavior, yet its RNA substrate signatures and membrane transport mechanism remain unclear. Here, we developed GlycoRNA-Lighted In situ Nano-Tracking (GLINT), an approach for the visualization of distinct RNA-specific glycosignatures. GLINT employs a modular, localized concatenated DNA circuit based on a proximity ligation-mediated dual hierarchical hybridization chain reaction (HCR). Metabolically labeled sialic acid probe and RNA-specific probes are combined into a dual-recognition module through proximity ligation. The module subsequently initiates a dual hierarchical HCR cascade, enabling ultrasensitive *in situ* tracking of U1, U3, U35a, Y5, and U8 glycoRNAs at the single-cell level. Leveraging GLINT technology, glycoRNAs were confirmed to be transported intracellularly via a SNARE protein-mediated secretory extracellular mechanism. Furthermore, the identification of ten subtypes of breast cancer cells was achieved based on the level of distinct RNA-specific glycosignatures on the cell surface. GLINT demonstrates great potential for tracking RNA-specific glycosignatures, offering a powerful tool for *in situ* cell subtyping and exploration of RNA-related glycosylation processes.

Graphical abstract

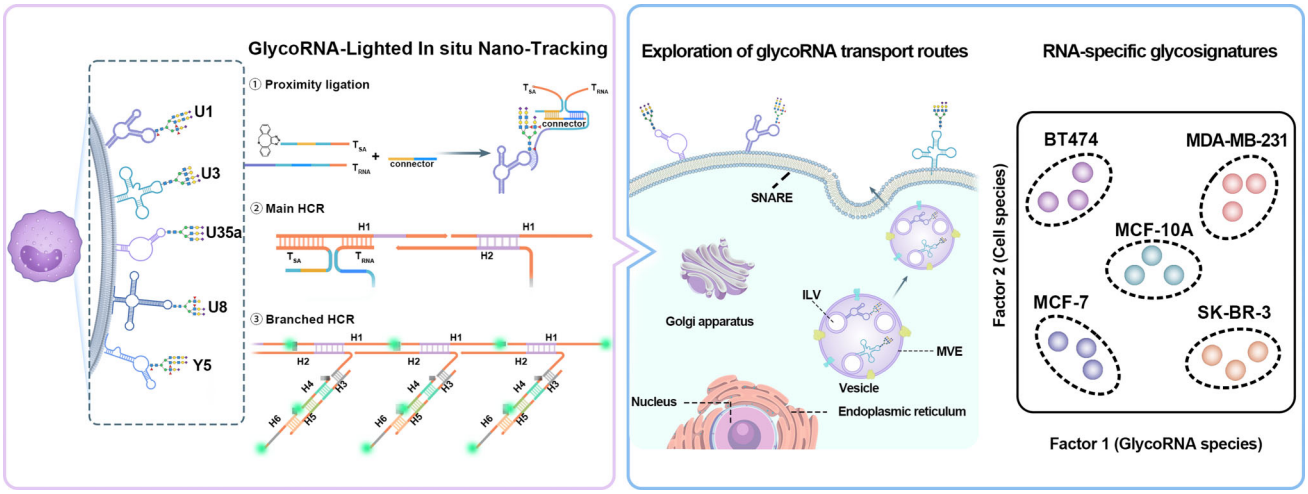

Introduction

The discovery of glycoRNA, a class of ribonucleic acid molecules modified through direct covalent linkage to glycan [1], has significantly expanded the research landscape of RNA biology. GlycoRNA exerts diverse biological functions through its glycan moiety [2], including the regulation of im-

Received: October 20, 2025. **Revised:** April 1, 2026. **Accepted:** April 6, 2026

mune and inflammatory responses [3], in addition to serving as a mediator in intercellular communication [4, 5]. GlycoRNAs on the tumor cell surface exhibit a highly abnormal glycoform [4, 6, 7], but their RNA substrate signatures remain unclear. Quantifying the differences in various glycoRNA expression levels and elucidating the heterogeneity of RNA moieties are crucial for deciphering the functions of glycoRNA and its regulatory roles in tumor progression. Furthermore, the low abundance of glycoRNA on the cell membrane poses a challenge for *in situ* detection, thereby hindering further mechanistic research [1].

The current methods for glycoRNA detection primarily emphasize glycan-specific analysis and metabolic labeling of glycans. Mass spectrometry-based glycan-specific analytical techniques [8] have been widely utilized for the characterization of glycan composition and conformation. Notably, the rPAL method [9] enables the specific enrichment of glycans through the formation of covalent bonds with aminated biotin probes. However, these methods require the extraction of glycoRNAs from the cells before analysis, rendering *in situ* detection unfeasible. To enable glycosylation labeling without the hydrolysis of glycan moieties, the metabolic glycan-labeling technique utilizing lectins has been developed for the detection of glycoRNAs in various species [10, 11]. However, lectins exhibit limited selectivity and specificity for glycoRNAs. Additionally, to achieve in-situ detection, the in-situ hybridization-mediated adjacent connection rolling circle amplification assay can be used to visualize the location and abundance of glycoRNA [6]. Another approach involves an enzyme-free system based on the conventional hybridization chain reaction (HCR) signal amplification and integrated with metabolic labeling for the quantitative detection of glycoRNA *N*-glycosylation sites [12]. The above methods offer certain analytical strategies for the in-situ visualization and localization of glycoRNA, but they are mainly suited for a single glycoRNA type and exhibit limited capability in distinguishing the heterogeneity among glycoRNA species.

Taking advantage of the programmable molecular design and flexible structural modulation, catalytic DNA circuits have emerged as a critical platform for the highly sensitive detection of trace substrate [13–15]. Among the various strategies for catalytic DNA circuits, the HCR is widely employed for detecting diverse biomolecules because of its isothermal and enzyme-free nature [16–18]. Through the precise engineering of initiators and hairpin probes, HCR enables highly specific discrimination of diverse biomolecules with exceptional accuracy, which facilitates high-resolution *in situ* imaging of multiple RNA species when utilized for multiplex RNA encoding [19, 20]. To enhance the efficiency of hybridization, HCR has been integrated with a catalytic hairpin assembly (CHA) to construct enzyme-free autocatalytic circuits for sensitive sensing of intracellular biomolecules, which significantly enhances the detection sensitivity for low-abundance RNA [21, 22]. However, the incorporation of multiple CHA hairpin components may considerably increase the risk of nonspecific hybridization and unintended signal leakage, potentially compromising detection accuracy [23, 24]. Thus, developing an ultrasensitive autocatalytic DNA circuit that dually targets glycans and RNA is essential to achieve high-fidelity *in situ* imaging of low-abundance glycoRNAs on cell membranes.

Herein, a glycoRNA-lighted *in situ* nano-tracking (GLINT) strategy is proposed based on a modular localized concatenated DNA circuit, enabling the elucidation of cell-surface RNA heterogeneity and transport mechanisms at the single-cell level. Only when glycoRNA is present can the metabolically labeled sialic acid probe and RNA-specific probe, respectively, recognize its glycan moiety and RNA part, and the dual-pivot gated connection chain can mediate the connection between the two probes. Subsequently, the forming connection complex can initiate the traditional HCR reaction containing H1 and H2. The unbound segment of H2 is then captured by H3 in the secondary layer HCR circuit, which sequentially activates the H3, H4, H5, and H6 probes and triggers the dual hierarchical HCR-mediated autonomous domino amplification effect [25–27]. GLINT achieves exponential cascade amplification of the products and realizes high-precision *in situ* imaging through the anchoring of low-diffusivity polymers. Moreover, GLINT is capable of detecting the expression levels of five glycoRNA species (U1, U3, U35a, Y5, and U8) in both normal breast epithelial cells and breast cancer cell lines through target probe replacement, thereby facilitating the identification of breast cancer cell subtypes and the analysis of RNA heterogeneity. Our strategy not only facilitates the elucidation of glycoRNA biological functions but also provides a robust platform for interdisciplinary research at the interface of glycobiology and RNA biology.

Materials and methods

Materials

Salmon sperm DNA (SSD) was purchased from Sigma-Aldrich. Ac_4ManNAz, NGI-1, kifunensine, swainsonine, and PNGase-F, NGI-1, O-glycosidase, swainsonine, were purchased from MedChemExpress. α2–3,6,8,9-neuraminidase A was purchased from New England BioLabs (NEB). Bovine serum albumin (BSA) was purchased from Aladdin. RNase T1, CT-B-AF647 were purchased from Thermo Fisher Scientific.VTl1B Polyclonal Antibody, TSNARE1 Polyclonal Antibody, and Donkey anti-Rabbit IgG (H + L) Highly Cross-Adsorbed Secondary Antibody were purchased from Invitrogen Life Technologies. Phosphate-buffered saline (PBS) and all culture media were purchased from Gibco. All the oligonucleotide sequences were purchased from Sangon Biotech. All other reagents and solvents were obtained from domestic suppliers and were used as received.

DNA polyacrylamide gel electrophoresis (PAGE)DNA

To verify the feasibility of the HCR reaction, T_{mimic}, T_{SA}, connector, T_{RNA}, and H1-H6 (Supplementary Table S1) were prepared at a concentration of 10 μM each. Subsequently, T_{mimic} (1 μL) and T_{SA} (1 μL), connector (1 μL), T_{RNA} (1 μL) were individually mixed with H1–H2 (3 μL, 10 μM), H3–H4 (2 μL, 10 μM), and H5–H6 (1 μL, 10 μM). The mixtures were then supplemented with buffer to achieve a final volume of 100 μL and incubated at 25°C for 2 h. Then the samples were diluted with loading buffer and loaded into a freshly-prepared 20% native polyacrylamide gel. Electrophoresis was conducted in 1 × TBE buffer at 110 V for 1 h. The gel was stained with GelRed (1:10 000) and imaged using a Bio-Rad ChemiDoc XRS System (Bio-Rad, USA).

Cell culture

MCF-7cells were obtained from China Center for Type Culture Collection (CTCC), while MCF-10A, SK-BR-3, MDA-

MB-231, BT549, Hs578T, HCC1806, MDA-MB-361, and MDA-MB-436 cells were purchased from Procell. BT474 cells were acquired from the Chinese Academy of Sciences (CAS). All cells were cultured at 37°C in a humidified incubator with 5% CO_2. MCF-7, SK-BR-3, Hs578T, MDA-MB-361, MDA-MB-436, and MDA-MB-231 cells were cultured in DMEM supplemented with 10% fetal bovine serum, 100 U/mL penicillin, and 100 U/mL streptomycin. MCF-10A was cultured in MCF-10A special medium. BT474, BT549, and HCC1806 were cultured in RPMI-1640 medium supplemented with 10% FBS, 100 U/mL penicillin, and 100 U/mL streptomycin.

Cytotoxicity test

A total of 10^5 cells were seeded in 96-well plates and incubated overnight at 37°C. Media containing 10, 20, 40, 50, 80, and 100 μM of Ac_4ManNAz were added to each well. One group was incubated for 24 h, and another group was incubated for 48 h. After incubation, 10 μL of CCK-8 solution was added to each well, followed by an additional incubation of the plates at 37°C for 1 h. Subsequently, the absorbance at 450 nM was measured using a microplate reader. The cell survival rate was calculated using the specified formula.

Optimization of reaction conditions

To determine the optimal conditions for GLINT, a fluorescence spectrophotometer was employed to optimize the reaction parameters. First, the fluorescent labeling strategy was optimized by labeling either two or three DNA strands in the HCR reaction with the fluorophore. The combination of H1, H4, and H6 labeled with fluorophore exhibited the most significant difference in fluorescence intensity between negative and positive groups. Next, the reaction concentration was optimized by evaluating the combinations of H1–H2, H3–H4, and H5–H6 at concentration ratios of 1:1:1, 1:2:2, 2:1:1, 2:2:1, 3:2:1, and 4:2:1. Notably, the 3:2:1 ratio yielded the largest fluorescence intensity difference. The reaction temperature was then optimized by measuring the fluorescence intensity at 20°C, 25°C, 30°C, 35°C, 37°C, and 40°C. Importantly, the most pronounced difference in fluorescence intensity was observed at 25°C. Finally, the reaction time was optimized by recording fluorescence intensity at 15 min intervals from 0 to 150 min.

Copper-free click conjugation to Ac4ManNAz

To prove the occurrence of click chemistry in the glycan part, flow cytometry analysis was performed. Cells incubated with Ac_4ManNAz for 48 h were then treated with 2 μM T_{SA} (modified with FAM) or unmodified DBCO for 1 h at 37°C.

In situ imaging of glycoRNA with HCR

To validate the feasibility of the GLINT system in cells, MCF-7 cells were seeded at a density of 10^5 per well in imaging dishes and cultured overnight. The medium was replaced with fresh medium containing 100 μM of Ac_4ManNAz, and the cells were incubated at 37°C for 48 h. After washing with PBS, SSD (1 μL of 10 μM), T_{SA} (1 μL of 10 μM), connector (1.5 μL of 10 μM), $T_{RNA\text{-}U1}$ (1 μL of 10 μM), BSA (1 μL of 25 μg/μL), and Tris–HCl buffer were added to a final volume of 100 μL. The cells were then incubated at 37°C for 1 h.

Subsequently, the cells were washed three times with PBS. Optimal proportions of H1-H6 were added, along with Tris–HCl buffer solution, to achieve a final volume of 100 μL. The cells were incubated at 37°C for 2 h. Finally, cells were washed and resuspended in PBS before being imaged with an ultra-high-resolution laser scanning confocal microscope (LSM880).

Validation of HCR specificityHCR

To validate the specificity of GLINT, we adjusted the expression levels of glycan and RNA in glycoRNAs. To digest the RNA moiety, live cells were incubated with 1 U/μL RNase T1 in 100 μL of HBSS at 37°C for 20 min, then analyzed using GLINT.

In addition, to verify the necessity of the glycan of glycoRNA for GLINT, MCF-7 cells were pre-treated with 8 μM NGI-1, 2 μM kifunensine, or 40 μM swainsonine for 24 h before glycoRNA imaging. In the enzymatic method, MCF-7 cells were incubated with PNGase-F, α2–3,6,8,9-neuraminidase A, or O-glycosidase at a concentration of 10 U per 100 μL in HBSS at 37°C for 30 min to facilitate the digestion of glycoRNA.

Atomic forces experiments

After the HCR reaction system was reacted based on the previously optimized conclusions, the sample was fixed on a cleaned and pre-treated mica sheet, followed by adjusting the parameters of the AFM, including the scanning range, scanning speed, etc. Finally, the sample was placed on the sample stage of the AFM and scanned with a probe to record the three-dimensional morphology information of the sample surface.

Lipid raft staining and immunofluorescence imaging

We used the Cell Plasma Membrane Staining Kit with DiD (Far-red Fluorescence) and an Alexa Fluor 647 lipid raft labeling kit (Thermo Fisher Scientific) to label lipid rafts.

According to the product manual, after being treated with GLINT, a PBS mixture containing 1 mg/mL of CTxB-AF647 was applied to the imaging dish, followed by incubation in ice water for 30 min. For the cell membrane far-red fluorescence staining, cells were incubated with the working solution at 37°C for 15 min and washed. After overnight culture under standard conditions, the medium was replaced with fresh medium containing 100 μM Ac_4ManNAz, and incubated at 37°C for an additional 48 h. Subsequently, the culture medium was removed, and the washed cells were washed three times with PBS. Then, the cells were covered with the primary antibody working solution (diluted 1:250 in 1% (w/v) BSA solution) and incubated at 4°C overnight. Following incubation, cells were washed five times with PBS. Then, the secondary antibody working solution (diluted 1:500 in 1% (w/v) BSA solution) was added, and cells were incubated at room temperature protected from light for 1 h for staining. After staining, cells were washed three times with PBS. Finally, GLINT analysis was performed on the cells.

To explore the synthetic pathway of glycoRNA, SNARE proteins were stained. After pretreatment of 10^6 cells/mL by the GLINT method, polyclonal antibodies (VTI 1B polyclonal antibody diluted 1:250, TSNARE 1 polyclonal antibody diluted 1:100) prepared in 1% BSA were added to the cells and incubated at 4°C overnight. The cells were washed five times with PBS and then stained with a 1:500 diluted donkey anti-

rabbit IgG (H + L) solution (prepared in 1% BSA) at room temperature for 1 h. After washing the cells three times, continue with the GLINT and observe under Ultra-high solution laser confocal (LSM880). The colocalization assay was performed with Coloc2 and JACoP plug-ins of Fiji (ImageJ).

siRNA-mediated gene silencingsirna

siRNAs targeting human VTI1B, TSNARE1, and GAPDH, as well as a non-targeting negative control siRNA, were synthesized by Sangon Biotech (Shanghai, China). The sequences are listed in Supplementary Table S1. MCF-7 cells in the logarithmic growth phase were seeded into six-well plates at a density of 1×10^5 cells per well in 2 mL of complete medium. When cells reached 30–50% confluence, transfection was performed using Lipofectamine™ RNAiMAX (Thermo Fisher Scientific) according to the manufacturer's instructions. The following experimental groups were included: blank control (untreated), negative control (transfected with NC siRNA), positive control (transfected with si-GAPDH), VTI1B knockdown (transfected with three independent si-VTI1B), and TSNARE1 knockdown (transfected with three independent si-TSNARE1). After transfection, cells were cultured at 37°C in a 5% CO_2 incubator. Cells were harvested at 48 h post-transfection for total RNA extraction and qPCR analysis, and at 72 h post-transfection for membrane protein extraction and Western blot validation.

Quantitative real-time PCR (qPCR)

Total RNA was extracted from each group using an RNA extraction kit (Sangon Biotech). RNA concentration and purity were measured using a NanoDrop spectrophotometer. A total of 1 μg RNA was reverse transcribed into cDNA according to the manufacturer's protocol. qPCR was performed using a SYBR Green qPCR kit on a real-time PCR system. The thermal cycling conditions were as follows: 95°C for 30 s; followed by 40 cycles of 95°C for 5 s and 60°C for 30 s.

Western Blot validation of knockdown efficiencyWestern Blot

At 72 h post-transfection, cells were washed three times with ice-cold PBS. Membrane proteins were extracted using a membrane protein extraction kit (Beyotime) according to the manufacturer's instructions. Protein concentrations were determined using a BCA protein assay kit (Beyotime). Samples were mixed with 5 × SDS loading buffer and denatured by boiling for 10 min.

Equal amounts of protein (30 μg per lane) were separated by SDS-PAGE and transferred onto PVDF membranes. Membranes were blocked with 5% non-fat milk for 2 h at room temperature, then incubated overnight at 4°C with primary antibodies as follows: rabbit monoclonal anti-VTI1B (1:1000, Thermo Fisher Scientific); rabbit monoclonal anti-TSNARE1 (1:1000, Thermo Fisher Scientific); rabbit monoclonal anti-Calnexin (1:1000, bioswamp) as a loading control.

After washing three times with TBST (10 min each), membranes were incubated with HRP-conjugated goat anti-rabbit secondary antibody (1:10 000, Thermo Fisher Scientific) for 1 h at room temperature. Membranes were washed again with TBST, and protein bands were visualized using an ECL chemiluminescence kit (Beyotime) and imaged with a gel documentation system. Band intensities were quantified using ImageJ software, and relative protein expression levels were normalized to Calnexin. All experiments were independently repeated three times.

Immunofluorescence imaging and Confocal colocalization analysis

MCF-7 cells in the logarithmic growth phase were seeded into confocal dishes at a density of 5×10^4 cells per well and transfected with siRNAs as described above. At 24 h post-transfection, Ac4ManNAz was added to the culture medium at a final concentration of 100 μM, and cells were cultured for an additional 48 h. Immunofluorescence colocalization was then performed as previously described.

Glycosignatures confocal Glycosignatures

To explore the relationship between glycoRNA and the classification of breast cancer cells, RNA targets that bind to five glycoRNAs (U1, U3, U35a, Y5, U8) were synthesized and applied to ten types of breast cancer cells. MCF-7, MCF-10A, BT474, SK-BR-3, MDA-MB-231, MDA-MB-361, BT549, Hs578T, MDA-MB-436, and HCC1806 were seeded at a density of 10^6 cells/mL in imaging dishes and cultured overnight. Replaced the medium with fresh medium containing 100 μM of Ac_4ManNAz tomorrow, and the cells were incubated at 37°C for 48 h. Then, the fluorescence intensity was observed under Ultra-high resolution laser confocal (LSM880) and quantified.

Data analysis

All experiments were performed with at least three biological replicates. For each individual biological replicate, three technical repeats were performed in cell imaging experiments. The results of each test are displayed as the mean ± SD. All the statistical calculations and graph making were performed with Origin or GraphPad9. For comparisons between two groups, a two-tailed unpaired Student's t-test was employed. For multiple group comparisons, one-way analysis of variance (ANOVA) followed by Tukey's post hoc test was used for multiple comparison correction. $P < 0.05$ (∗), $P < 0.01$ (∗∗), $P < 0.001$ (∗∗∗), and $P < 0.0001$ (∗∗∗∗). Data processing and statistical analyses were performed using Origin for cluster analysis, and the R programming language for unsupervised hierarchical clustering, leave-one-out cross-validation (LOOCV), and permutation tests.

Results

Working principle of the GLINTGLINT

The principle of the proposed modular localized concatenated DNA circuit is illustrated in Scheme 1. The process of *in situ* visualization of glycoRNAs is achieved by a double biorecognition unit and a concatenated dual hierarchical HCR catalytic circuit. The biorecognition module includes three sequences (Scheme 1A): (1) a glycan-binding azadibenzocyclooctyne-amine (DBCO)-functionalized DNA strand (T_{SA}), which can specifically bind to a glycan group via click chemistry following the attachment of an azide group (N_3) to the glycan. T_{SA} contains a joining chain linker (linker A) for subsequent nucleic acid hybridization, a spacer to avoid steric hindrance during hybridization, and a DNA linker (a') for subsequent HCR; (2) an RNA complementary probe (T_{RNA}) with a DNA strand for RNA

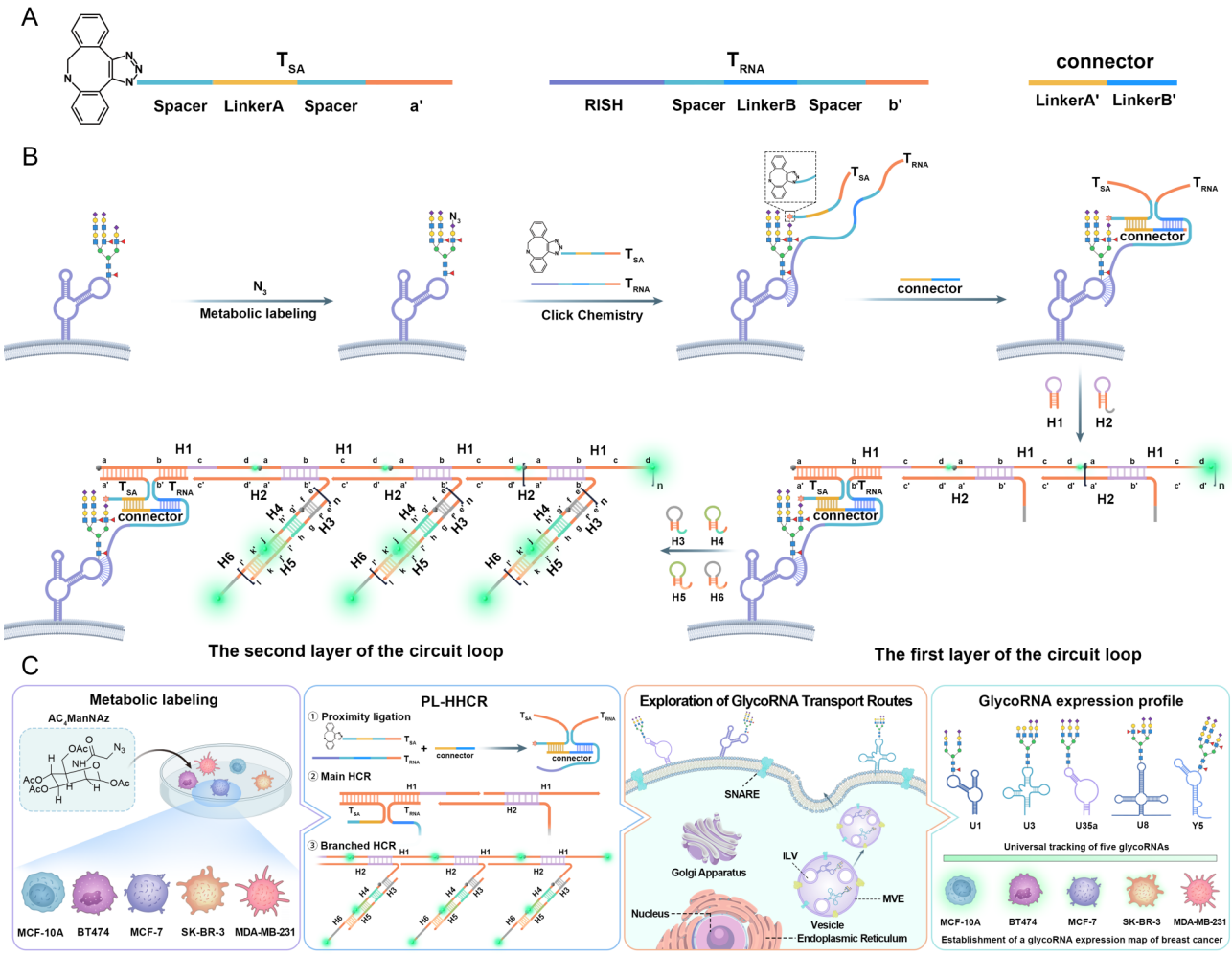

Scheme 1. Schematic illustration of glycoRNA *in situ* imaging based on the GLINT strategy and its application. (**A**) Structure and functional domains of the T_{SA}, T_{RNA}, and connector. (**B**) Mechanism insights into GLINT-mediated glycoRNA recognition and signal amplification. (**C**) Application workflow and functional characterization of GLINT in cells..

in situ hybridization (RISH), two spacers, a joining chain linker (linker B), and a DNA linker (b') for subsequent HCR; (3) a dual-pivot gated connector chain (connector), which is complementary to the bases of T_{SA} and T_{RNA}. As shown in Scheme 1A, the detection of glycoRNAs occurs only when the dual recognition of glycan and RNA triggers connector hybridization. Then, the excess DNA strands of T_{SA} and T_{RNA} (a', b') are captured by H1 and subsequently undergo the first layer of HCR with the involvement of H1 and H2. Next, the 3′ end of the H2 hairpin recognizes and opens H3 through specific recognition, initiating a secondary layer HCR cascade. The successive cross-opening of H1, H4, and H6 leads to the continuous separation of the fluorophore donor/acceptor pairs (FAM/TAMRA) to effectively generate a "turn-on" fluorescence output.

Feasibility verification of GLINT for glycoRNA detectionGLINT

To validate the feasibility of the dual hierarchical HCR component within this strategy, we first employed polyacrylamide gel electrophoresis (PAGE) to investigate whether the H1–H6 sequences were capable of undergoing dual hierarchical HCR. After H1–H6 was incubated with the H1 mimetic complementary strand (T_{mimic}) at 25°C for 2 h, electrophoresis was performed. A distinct new band appeared above H1–H6 and T_{mimic} (Supplementary Fig. S2A, lane 8), confirming the successful occurrence of a dual hierarchical HCR, which led to the formation of amplification products with higher molecular weights. Next, the feasibility of the proximity-induced reaction was validated. T_{SA}, T_{RNA}, and connector components, as well as T_{SA}, T_{RNA}, connectors, and H1–H6 complexes, were incubated at 25°C for 2 h, respectively. As illustrated in Fig. 1A, T_{SA}, $T_{RNA\text{-}U1}$, and the connector are capable of hybridizing to form a stable complex (lane 5). Furthermore, in the presence of H1-H6, this complex can trigger the DNA circuit amplification reaction, leading to the appearance of a clear amplification band at the top of lane 6. In addition, to evaluate the assembly kinetics of the dual-recognition module and the orthogonality of the dual-layered HCR, we performed fluorescence quenching kinetics and cross-reactivity assays, respectively. In the fluorescence quenching kinetics assay, we used BHQ-labeled T_{SA} and FAM-labeled $T_{RNA\text{-}U1}$ to monitor the fluorescence change in the presence of the target in real-time. By fitting the kinetic curves with a single-exponential decay model, the assembly rate constant of the dual-recognition module was determined to be $k = 0.132 \pm 0.015$ min^{-1} (mean ± SD, $n = 3$), corresponding to a half-life of $t_1/_2$

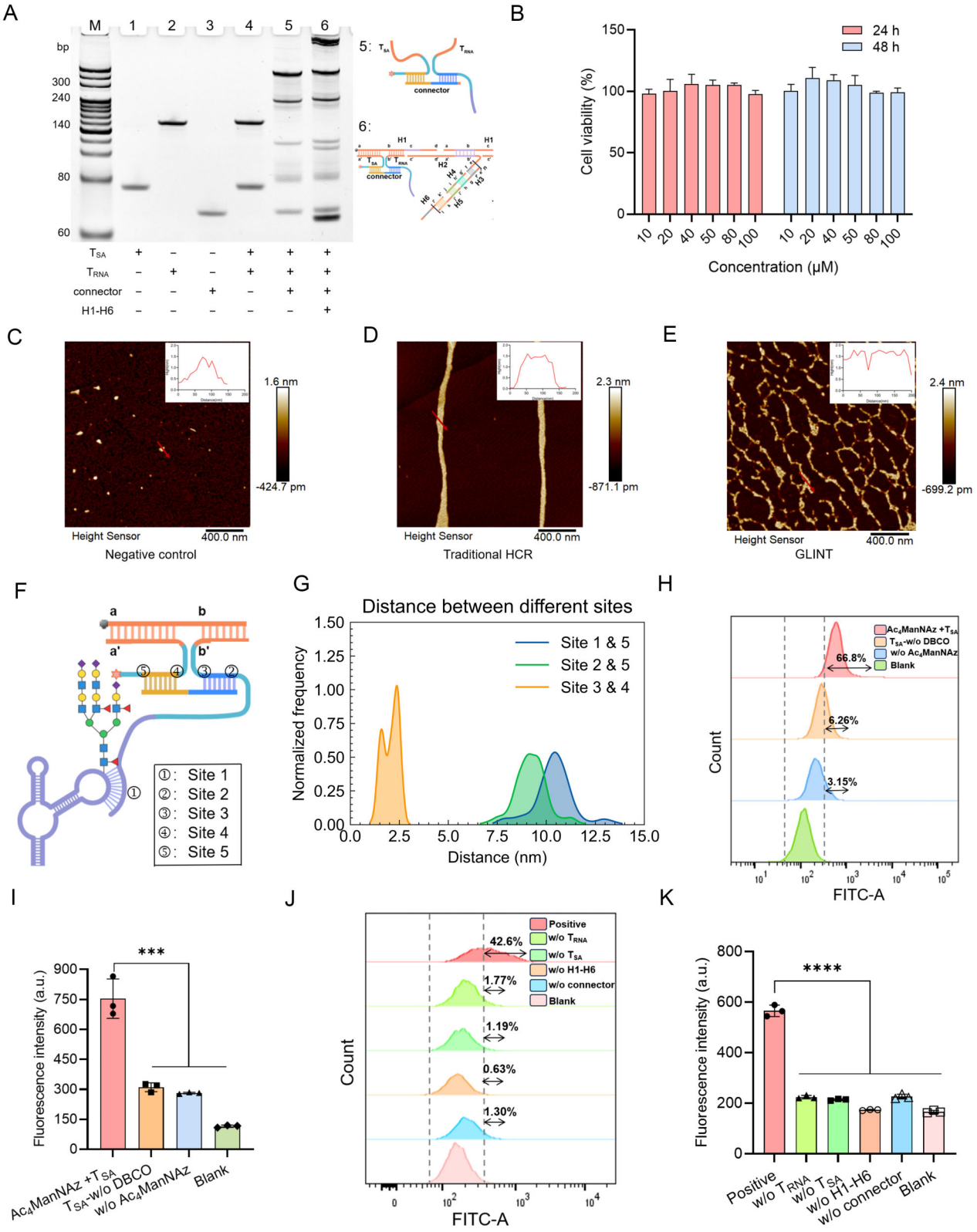

Figure 1. Validation of GLINT feasibility. (**A**) Confirmation of GLINT occurrence *in vitro* through PAGE-based analysis. (**B**) Toxicity assessment of Ac_4ManNAz in MCF-7 Cells. (**C**) Occurrence of the GLINT reaction was characterized using AFM in the absence of T_{mimic}. (**D**) The occurrence of the traditional HCR reaction and the generated DNA products were characterized by AFM. (**E**) The occurrence of the GLINT reaction and the generation of high-molecular-weight dsDNA products were characterized using AFM in the presence of T_{mimic}. (**F**) Schematic representation of the GLINT system depicting the selected sites (Sites 1–5) for distance analysis. (**G**) The distribution of distances between sites of interest. (**H**) MCF-7 cell clustering to verify the feasibility of the dual recognition component in the GLINT system using flow cytometry. (**I**) The average fluorescence intensity (a.u.) of cells in (**H**). (**J**) Flow cytometry verified the feasibility of the GLINT system in cells. (**K**) The average fluorescence intensity (a.u.) of cells in (**J**). (**H**) and (**J**) represent two independent experiments, respectively. Data are shown as mean ± SD ($n = 3$). Statistical significance was determined by an independent-samples t-test; $^{***}P < 0.001$; $^{****}P < 0.0001$.

= 5.24 ± 0.60 min. These results indicate that the dual-recognition module can complete half-assembly in approximately 5 min in the presence of the target, demonstrating rapid reaction kinetics (Supplementary Fig. S4C). To verify the orthogonality of the dual hierarchical HCR, we compared the *in vitro* fluorescence intensities of the complete reaction system (H6 labeled with FAM), the H6 single-strand control group, and the no-initiator control group. The results showed that significant fluorescence signals were observed only in the complete reaction system, confirming that the dual hierarchical HCR has high orthogonality with no obvious cross-reaction (Supplementary Fig. S2B).

To determine the optimal reaction conditions for GLINT, we systematically evaluated several crucial parameters, including fluorescent labeling sites, probe concentrations (H1–H6), reaction temperature, and reaction time (Supplementary Fig. S3A-F). Through the use of hairpin combinations labeled with distinct fluorescent groups at specific modification sites to initiate GLINT, the most intense fluorescence signal was detected when the fluorescent labeling was applied to the H1, H4, and H6 combinations. Furthermore, the effect of varying hairpin concentrations was investigated. The maximum difference in fluorescence intensity between the positive and negative GLINT groups was observed when the concentration ratios of H1-2, H3-4, and H5-6 hairpins were set to 300, 200, and 100 nM, respectively. The reaction temperature and time were optimized similarly. Eventually, we chose 25°C (Supplementary Fig. S3G) and 15 min (Supplementary Fig. S4A) as the optimal conditions for the reaction. After determining the optimal reaction conditions for GLINT, the concentration gradient of T_{mimic} was established as 0, 10^2, 10^3, 10^4, 10^5, 10^6, 10^7, and 10^8 fM to evaluate the sensitivity of the detection method *in vitro*. The results demonstrated that the limit of detection of the method was 47.85fM (Supplementary Fig. S4B). Compared with recently published HCR-related studies [28–30], the *in vitro* detection limit of GLINT is significantly superior to other existing techniques (Supplementary Table S3). Under the optimal conditions, atomic force microscopy (AFM) was used to characterize the generated dsDNA products. Linear DNA structures of microscale size were observed when the T_{mimic} triggered dual hierarchical HCR, whereas only small fluorescent spots corresponding to the hairpin species were detected in the absence of T_{mimic} (Fig. 1C, E). Further comparison of the GLINT system with the products of traditional HCR (Fig. 1D) showed that traditional HCR only produced a small amount of linear structures and no branches. These results indicate that the GLINT system has excellent structural assembly ability, and its signal amplification efficiency is significantly superior to that of traditional HCR. Furthermore, the structure of GLINT was predicted using molecular dynamics simulations (Supplementary Fig. S1, Supplementary Table S2), which showed the assembly of the glycan probe, RNA-binding probe, and connectors. Fig. 1F, G shows the distance between the initial end of the T_{SA} and the middle region of the RNA-binding site (sites 1 and 5), the distance between the terminal ends of the T_{SA} and T_{RNA-U1} binding connectors (sites 3 and 4), and the distance between the initial ends of the T_{SA} and T_{RNA-U1} binding connectors (sites 2 and 5). Sites 1 and 5 are 7–14.5 nm apart, averaging 10.75 nm. Sites 3 and 4 are 1–3 nm apart, averaging 2 nm. Sites 2 and 5 are 6.5–12 nm apart, averaging 9.25 nm. Considering ssDNA bending and folding, the results match the connector dsDNA length (30 nt, ~9.86 nm), which indicates that the distances among the three DNA strands are all within 15 nm, demonstrating that the dual recognition modules can be successfully assembled through proximity connection.

To evaluate the feasibility of *in situ* imaging of the GLINT strategy in cells, GLINT was applied to breast cancer cells (MCF-7). We established six concentration gradients (10, 20, 40, 50, 80, and 100 μM) and incubated them with MCF-7 cells for 24 and 48 h, respectively. Analysis of cell viability across the tested concentrations and time points revealed no statistically significant differences among the treatment groups (Fig. 1B). Therefore, the incubation of cells with 100 μM Ac_4ManNAz for 48 h was determined as the suitable condition for subsequent cell experiments. To verify whether the glycoRNA on the MCF-7 cell membrane can undergo a click chemical reaction with T_{SA} after being metabolically labeled with N_3, MCF-7 cells were incubated in a culture system containing fluorescently labeled T_{SA} (T_{SA}-Fluor) for 1 h. Subsequently, flow cytometry was used to quantitatively analyze the fluorescence positivity rate and mean fluorescence intensity of cells. The results demonstrated that the fluorescence positivity rate reached 75.83% (Fig. 1H, I; Supplementary Fig. S5A). The difference in fluorescence intensity between the positive and negative control groups was statistically significant ($P < 0.001$), confirming the successful occurrence of the click chemical reaction and supporting the presence of N_3-labeled glycoRNA on the cell membrane surface. We further validated the feasibility of GLINT in cells using flow cytometry and assessed the necessity of its components, including Ac_4ManNAz, T_{SA}, T_{RNA-U1}, and the connector. The results showed a fluorescence positivity rate of 42.6%, and the difference in fluorescence intensity between the positive and negative control groups was statistically significant ($P < 0.0001$; Fig. 1J, K; Supplementary Fig. S5B).

GLINT for *in situ* imaging of glycoRNA in MCF-7 cells

We then employed GLINT in combination with confocal laser-scanning microscopy (CLSM) to visually detect the representative target U1 glycoRNA. As shown in Fig. 2A, bright signals from GLINT appeared on the membranes of MCF-7 cells in the positive group. When GLINT was conducted without Ac_4ManNAz, T_{SA}, T_{RNA-U1}, connector, or H1-H6, the signals were reduced by 6-, 5-, 5-, 6-, or 148-fold, respectively, demonstrating the necessity for all components (Fig. 2B). Next, we optimized both the reaction time of the confocal experiment and the DNA strands involved in the dual hierarchical HCR circuit, confirming that the maximum fluorescence intensity was achieved after incubation at 37°C for 2 h following the addition of six DNA strands (Supplementary Fig. S6A–D).

To optimize the binding stability and validate the specificity of the dual-recognition module, we systematically optimized the T_{RNA-U1} and T_{SA} probes, respectively. For T_{RNA-U1}–glycoRNA binding, a series of T_{RNA-U1} probes with varying numbers of complementary bases to glycoRNA were designed. Confocal imaging experiments revealed that optimal binding was achieved when the complementary region consisted of 17 bases (Supplementary Fig. S7A, B). In addition, the length of the spacer region in the T_{RNA-U1} probe was optimized, with 15 bases yielding the highest performance (Supplementary Fig. S7C, D). For T_{SA}–glycoRNA binding, we designed a non-binding control (non-T_{SA}) and a series of T_{SA} mutants containing different numbers of mismatched bases.

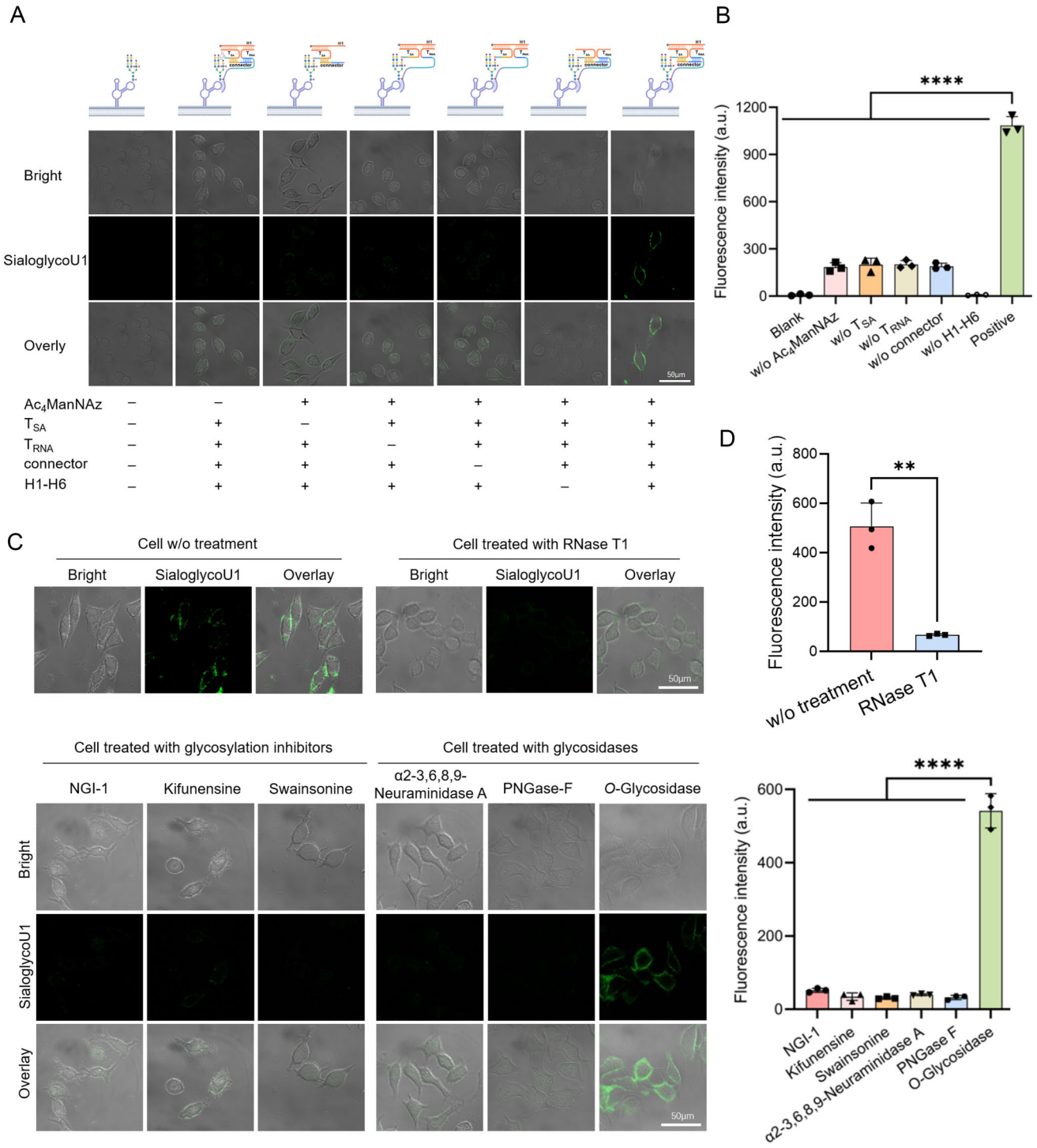

Figure 2. Assessment of the GLINT system for glycoRNA imaging in MCF-7 cells. (**A**) Confocal laser-scanning microscopy (CLSM) images of glycoRNAs using GLINT and various control groups in the absence of components for GLINT; w/o, without. (**B**) Quantification of average fluorescence intensity (a.u.) per cell in (**A**). Data are shown as mean ± SD ($n = 3$). ****$P < 0.0001$. (**C**) Specificity verification of GLINT. Live MCF-7 cells were respectively treated with RNAase T1, glycosylation inhibitor, and glycosidase, then analyzed by GLINT. (**D**) Quantification of average fluorescence intensity (a.u.) per cell in (**C**). Data are shown as mean ± SD ($n = 3$), **$P < 0.01$, ****$P < 0.0001$.

Cells were treated with mixtures of T_{SA} and non-T_{SA} at various ratios. The results showed that increasing the proportion of non-T_{SA} led to a gradual decrease in fluorescence intensity (Supplementary Fig. S8A, B). Similarly, a higher number of mismatched bases in T_{SA} resulted in weaker fluorescence signals (Supplementary Fig. S8C, D). These findings collectively confirm the specificity of T_{SA}–connector binding.

To verify whether the GLINT sensor can perform semi-quantitative analysis of glycoRNAs, we modulated the abundance of glycoRNAs using inhibitor-based and enzymatic digestion approaches. As shown in Fig. 2C, D, living cells were co-incubated with RNase T1 at 37°C for 20 min, followed by detection using the GLINT imaging technique. The results indicated that RNase T1 treatment resulted in a substantial 87% decrease in glycoRNA signal intensity relative to the untreated control group. These findings confirm that cell-surface RNA is a critical prerequisite for GLINT signal generation. After treating cells with N-linked glycosylation inhibitor 1 (NGI-1), kifunensine, or swainsonine for 24 h, the signal intensity of GLINT decreased by 90%, 94%, and 94%, respectively, compared to the untreated group. These findings confirm the specific recognition of glycoRNA polysaccharide structures. Additionally, living cells were treated with glycosidases known to cleave glycoRNA polysaccharides, namely, PNGase-F and α2–3,6,8,9-neuraminidase A. The results revealed that, compared to the control group, the signals in the PNGase-F group and the α2–3,6,8,9-neuraminidase A group decreased by 94% and 93%, respectively, further substantiating the critical role of glycan components in signal generation. As a control, cells treated with *O*-glycosidase, an enzyme incapable of cleaving glycoRNA polysaccharide structures, exhibited significant fluorescence. The collective results of the aforementioned experiments demonstrate that GLINT specifically recognizes glycan moieties associated with glycoRNA. Collectively, GLINT enables the highly specific and selective *in situ* visualization of glycoRNA.

Visualization of glycoRNA spatial distribution and transmembrane transport mechanism with GLINT

The red lipid membrane fluorescent probe DiD (DiD channel) is a carbocyanine-based fluorescent probe frequently employed for labeling the plasma membrane in live cells, with the ability to specifically anchor to the plasma membrane. We co-applied DiD and GLINT to cells and performed imaging analysis using an ultra-high-resolution laser confocal microscope. The results revealed significant co-localization between the fluorescence signals of DiD and GLINT, with a Pearson correlation coefficient of 71% [31] (Fig. 3A, B). In addition, it has been reported that glycoRNA and lipid rafts co-localize. To investigate their spatial distribution at the subcellular level, we employed GLINT for fluorescence imaging to analyze the distribution of glycoRNA and lipid rafts. The cholera toxin B subunit (CT-B), labeled with Alexa Fluor 647, was used to specifically mark lipid raft structures. Confocal imaging analysis revealed significant spatial co-localization between glycoRNA signals and CT-B-labeled lipid rafts (Fig. 3C, D). The Pearson correlation coefficient between GLINT and CT-B was 55%. Therefore, co-localization analysis of the GLINT signal with both DiD and CT-B signals suggests that glycoRNA is specifically localized to the lipid rafts of the cell membrane.

Previous studies [6, 32] have indicated that the intracellular trafficking of glycoRNA relies on SNARE-mediated vesicle exocytosis and membrane fusion, ultimately localizing to the cell surface. We employed GLINT to validate this hypothesis. In our experiments, SNARE proteins were stained with specific antibodies, and glycoRNA within the cells was imaged and analyzed using GLINT (Fig. 3E, F). The results revealed significant co-localization between glycoRNA and both the target SNARE protein (t-SNARE; TSNARE1) and the vesicle SNARE protein (v-SNARE; VTI1B), with a Pearson correlation coefficient of 49%. To further clarify the colocalization relationship between SNARE proteins and glycoRNA, siRNA was used to silence the genes encoding SNARE proteins. After verifying the knockdown efficiency by qPCR (Fig. 4A, D) and Western blot (Fig. 4B, C, E, F), immunofluorescence colocalization assays of SNARE proteins and glycoRNA were performed in the knockdown cells. Confocal microscopy results showed that the Pearson's correlation coefficients between glycoRNA and VTI1B/TSNARE1 were reduced to 0.04% and 0.12%, respectively, after knockdown (Fig. 4G, H). These results indicate that the intracellular transport of glycoRNA depends on the vesicle secretion and membrane fusion pathways mediated by VTI1B and TSNARE1.

Application of GLINT in glycoRNA visualization studies of breast cancer transformation

To investigate the correlation between glycoRNA expression profiles and the molecular subtypes and malignant progression of breast cancer, we selected 10 representative cell lines spanning multiple subtypes (Supplementary Table S4): normal mammary epithelial (MCF-10A, as negative control), Luminal A (MCF-7), Luminal B/HER2-overexpressing (BT-474, SK-BR-3, MDA-MB-361), and triple-negative breast cancer (TNBC) (BT549, Hs578T, MDA-MB-436, MDA-MB-231, HCC1806). The selection was also guided by the Fudan classification system—a four-subtype scheme based on Chinese breast cancer cohorts proposed by Shao and colleagues—to ensure clinical relevance. The RISH component of T_{RNA} was designed based on five glycoRNAs (U1 (snRNA), U3 (snoRNA), U8 (snoRNA), U35a (snoRNA), and Y5 (Y RNA)), and the expression levels of various glycoRNAs on the cell surface were subsequently detected using GLINT.

First, we confirmed that Ac_4ManNAz was not cytotoxic to all cell lines (Supplementary Fig. S9A–D). Using GLINT combined with confocal laser scanning microscopy (CLSM) and quantitative fluorescence analysis, we profiled surface glycoRNA expression in these cell lines. We found that the overall expression level of cell surface glycoRNAs exhibited a general downward trend with increasing malignancy grade, which was consistent with the findings of previous studies. Notably, the glycoRNA expression level in TNBC cell lines was generally low, suggesting a potential link between glycoRNA downregulation and the aggressive phenotype of TNBC. (Fig. 5A–E).

GLINT for distinguishing breast cancer subtypes and revealing glycoRNA heterogeneity

To investigate whether glycoRNA expression profiles correlate with breast cancer molecular subtypes, and to validate the ability of GLINT to distinguish subtype-specific glycoRNA signatures, we performed principal component analysis (PCA), unsupervised hierarchical clustering, and supervised classification modeling based on fluorescence quantification data from five target glycoRNAs (Fig. 6A).

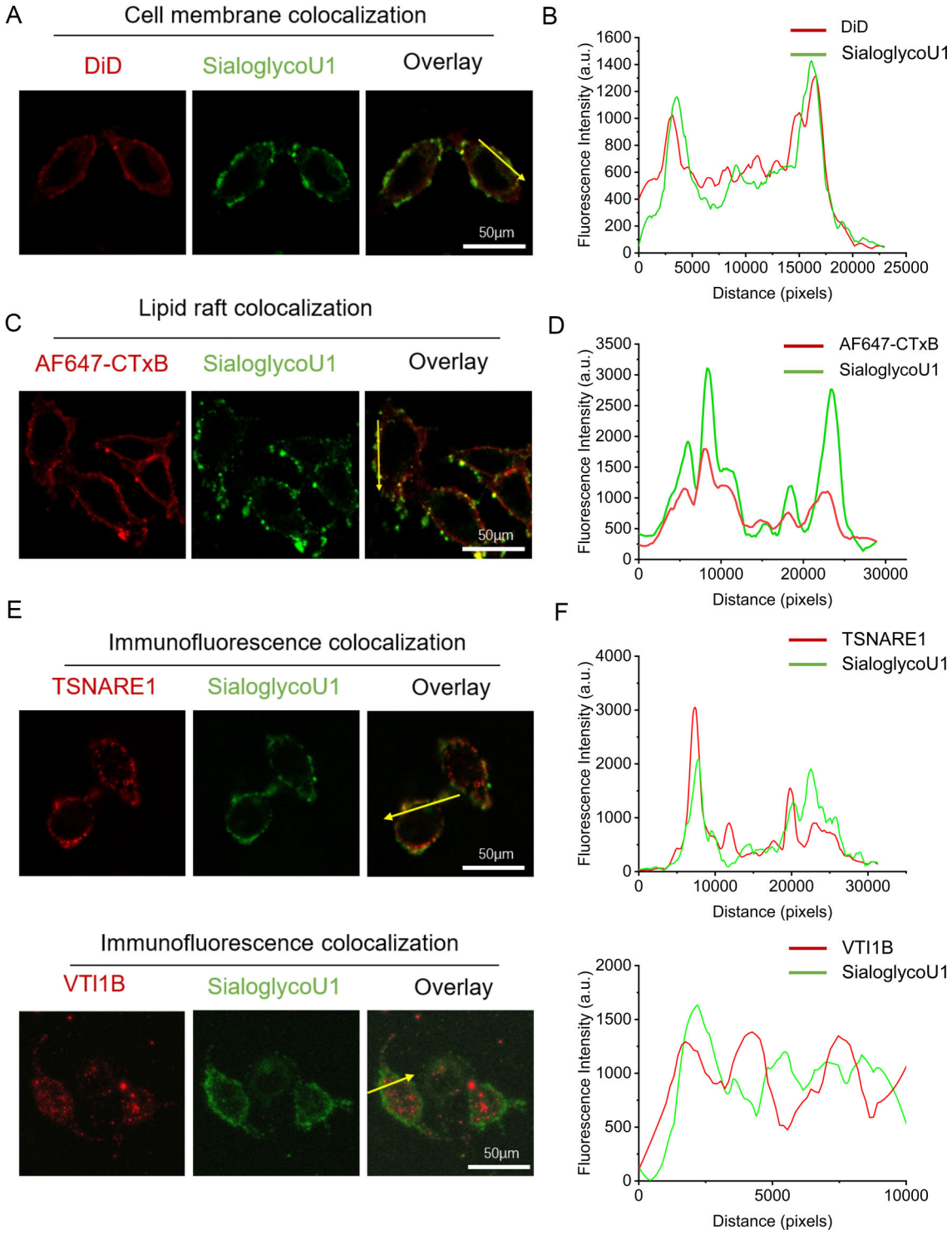

Figure 3. Spatial distribution of glycoRNA revealed by GLINT in MCF-7 cells. (**A**) Co-localization of the cell membrane (DiD channel) and glycoRNAs (FAM channel), imaged by GLINT with $T_{RNA\text{-}U1}$. (**B**) The fluorescence intensity line graph of co-localization corresponding to (**A**). (**C**) The co-localization image of lipid rafts (AF647-CTxB channel) and glycoRNAs (FAM channel), imaged by GLINT with $T_{RNA\text{-}U1}$. (**D**) The fluorescence intensity line graph of co-localization corresponding to (**C**). (**E**) Co-localization of t-SNARE (TSNARE1 channel) and v-SNARE (VTI1B channel) with GLINT-labeled glycoRNAs in the images (FAM channel), revealing the intracellular transport process of glycoRNAs. (**F**) The plot profiles show co-localization of glycoRNAs with t-SNARE or v-SNARE.

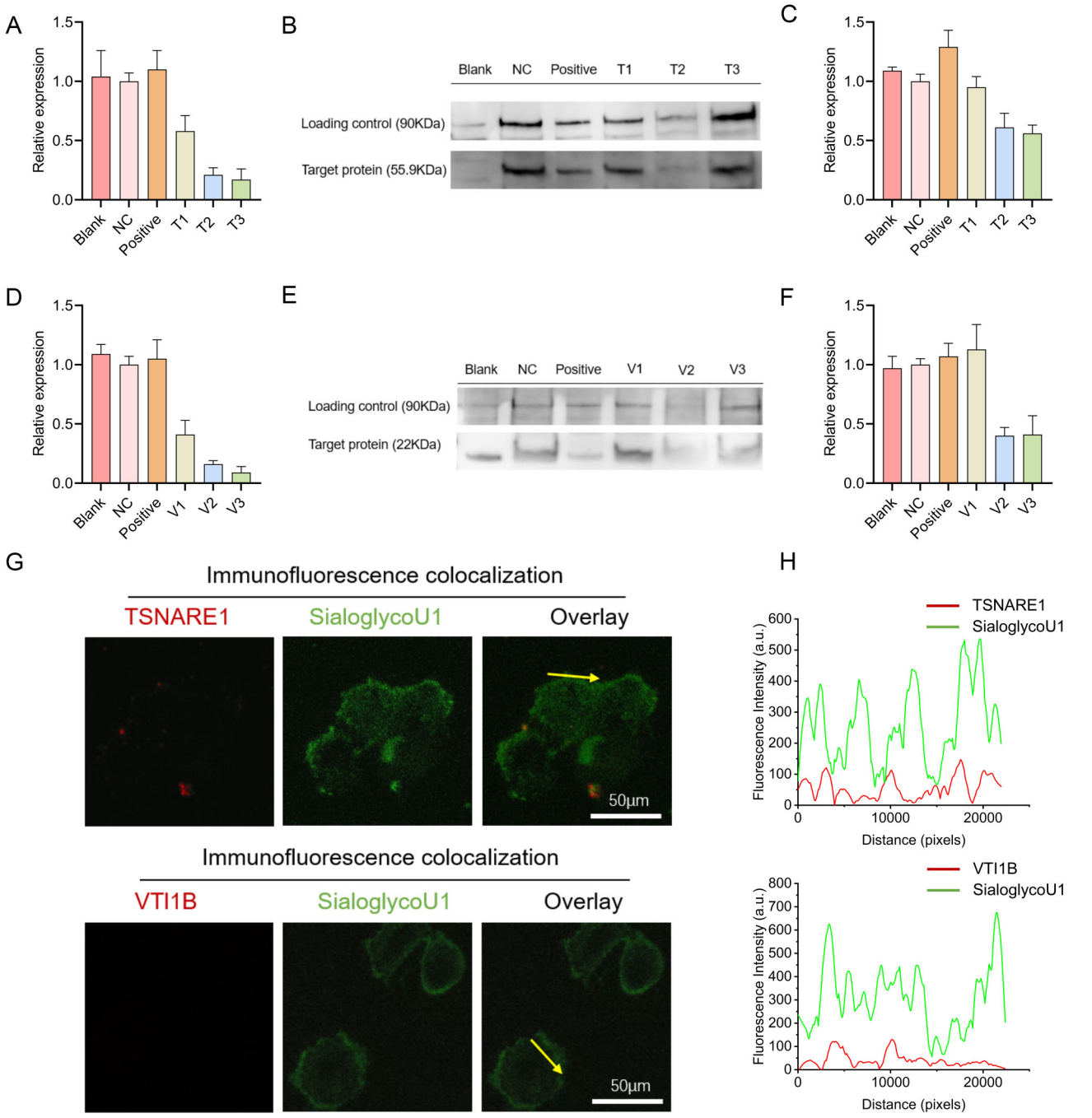

Figure 4. SNARE protein knockdown verification and colocalization analysis with glycoRNA. (**A**) Relative mRNA expression of v-SNARE protein after siRNA-mediated knockdown was determined by quantitative real-time PCR (qPCR). (**B**) Protein expression levels of v-SNARE protein were detected by Western blot. (**C**) Quantitative analysis of Western blot result(**B**). (**D**) Relative mRNA expression of t-SNARE protein after siRNA-mediated knockdown was determined by quantitative real-time PCR (qPCR). (**E**) Protein expression levels of t-SNARE protein were detected by Western blot. (**F**) Quantitative analysis of Western blot result (**E**). Data are presented as mean ± SD ($n = 3$). (**G**) Co-localization of t-SNARE (TSNARE1 channel) and v-SNARE (VTI1B channel) with GLINT-labeled glycoRNAs in the images (FAM channel). (**H**) The plot profiles show co-localization of glycoRNAs with t-SNARE or v-SNARE.

PCA revealed that the first two principal components explained 93% of the total variance in the dataset (87% by PC1 and 6% by PC2), capturing the majority of glycoRNA expression signature across the 10 cell lines. In the PCA score plot, biological replicates from the same cell line clustered tightly, while cell lines of different molecular subtypes and malignant grades were clearly separated. These results collectively demonstrated that glycoRNA expression patterns are subtype-specific (Fig. 6C). Unsupervised hierarchical clustering further confirmed these findings. Without any prior labeling, all samples were accurately grouped by their glycoRNA expression profiles, with all three biological replicates from each cell line forming a single distinct cluster. The clustering results were highly consistent with the molecular subtype and malignant grade of each cell line, providing further evidence that glycoRNA expression differs systematically across breast cancer subtypes (Fig. 6B).

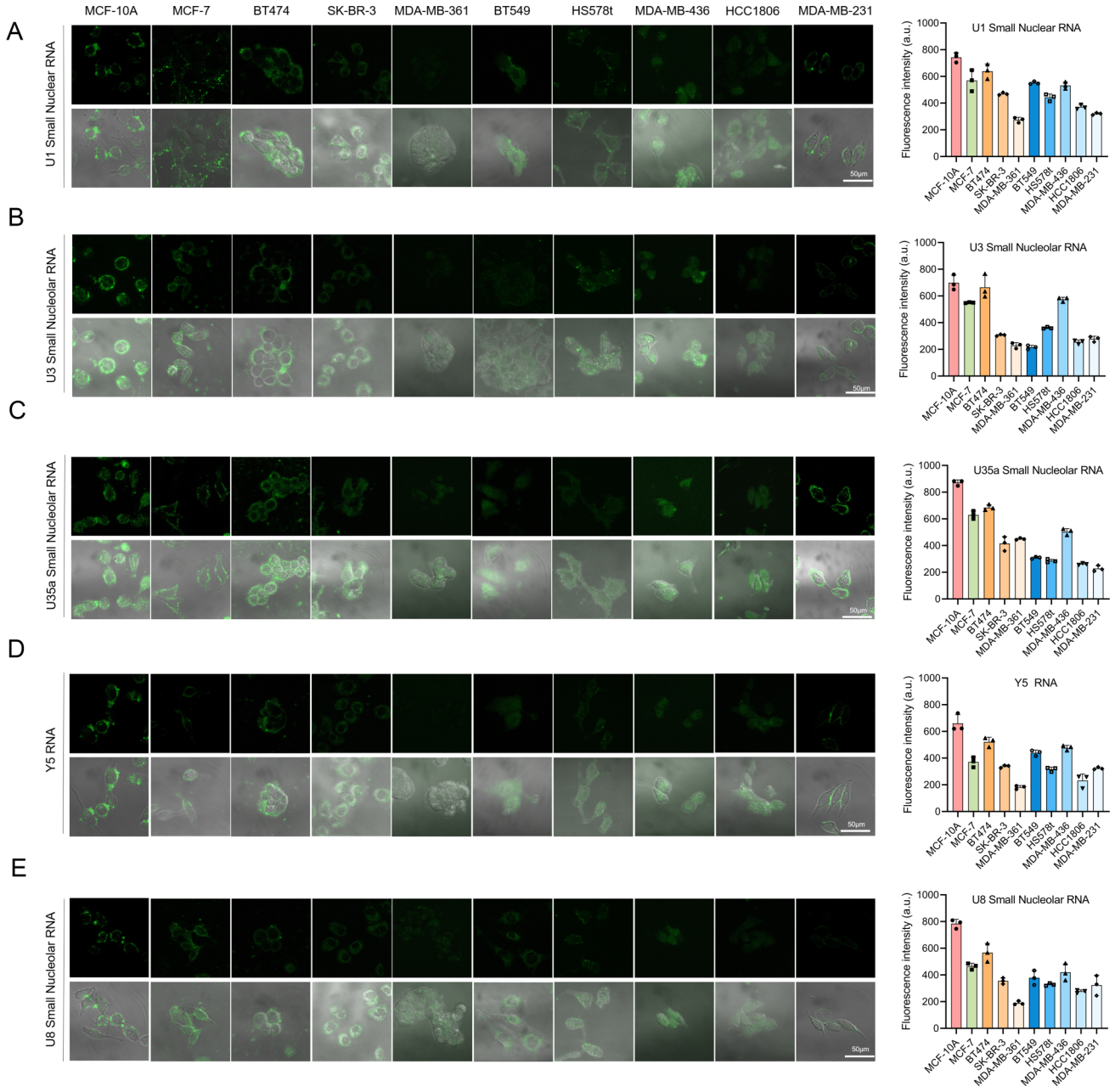

Figure 5. GLINT visualization of glycoRNA content changes during breast cancer malignant transformation. (**A–E**) Confocal images and single-cell fluorescence histograms of MCF-10A, MCF-7, BT474, SK-BR-3, MDA-MB-361, BT549 HS578t, MDA-MB-436, HCC1806, and MDA-MB-231 cells obtained via GLINT combined with $T_{RNA\text{-}U1}$, $T_{RNA\text{-}U3}$, $T_{RNA\text{-}U35a}$, $T_{RNA\text{-}Y5}$, $T_{RNA\text{-}U8}$.

Building on these observations, we built a breast cancer subtype classifier using a random forest algorithm and systematically validated its performance via leave-one-out cross-validation (LOOCV). Feature importance analysis identified U35a and U1 as the core glycoRNAs driving subtype classification, with the highest contribution to model performance (Fig. 6D), suggesting their critical roles in distinguishing breast cancer subtypes. LOOCV demonstrated that the glycoRNA-based classifier achieved high classification accuracy across the 10 breast cancer cell lines, with a mean accuracy of 0.92 ± 0.12, mean precision of 0.93 ± 0.09, mean recall of 0.92 ± 0.12, and a mean false positive rate of 0.01 ± 0.01. Quantitatively confirming this outstanding performance, the confusion matrix (Fig. 6E) showed that all 30 biological replicates (10 cell lines $\times$ 3 replicates) were correctly assigned to their respective identities, with zero misclassifications observed. To evaluate the statistical significance of the association between glycoRNA expression profiles and breast cancer cell subtypes, we performed a permutation test. By randomly shuffling cell subtype labels, we constructed 10 000 permutation models. The average accuracy of the permutation models was only 6.24%, with 95% of the permutation models achieving accuracies below 20%. The accuracy of all permutation models was significantly lower than that of the true model, with a permutation test P-value of < 0.0001. These results demonstrate that the association between glycoRNA expression profiles and breast cancer cell subtypes is highly statistically significant and not due to random chance, further high-

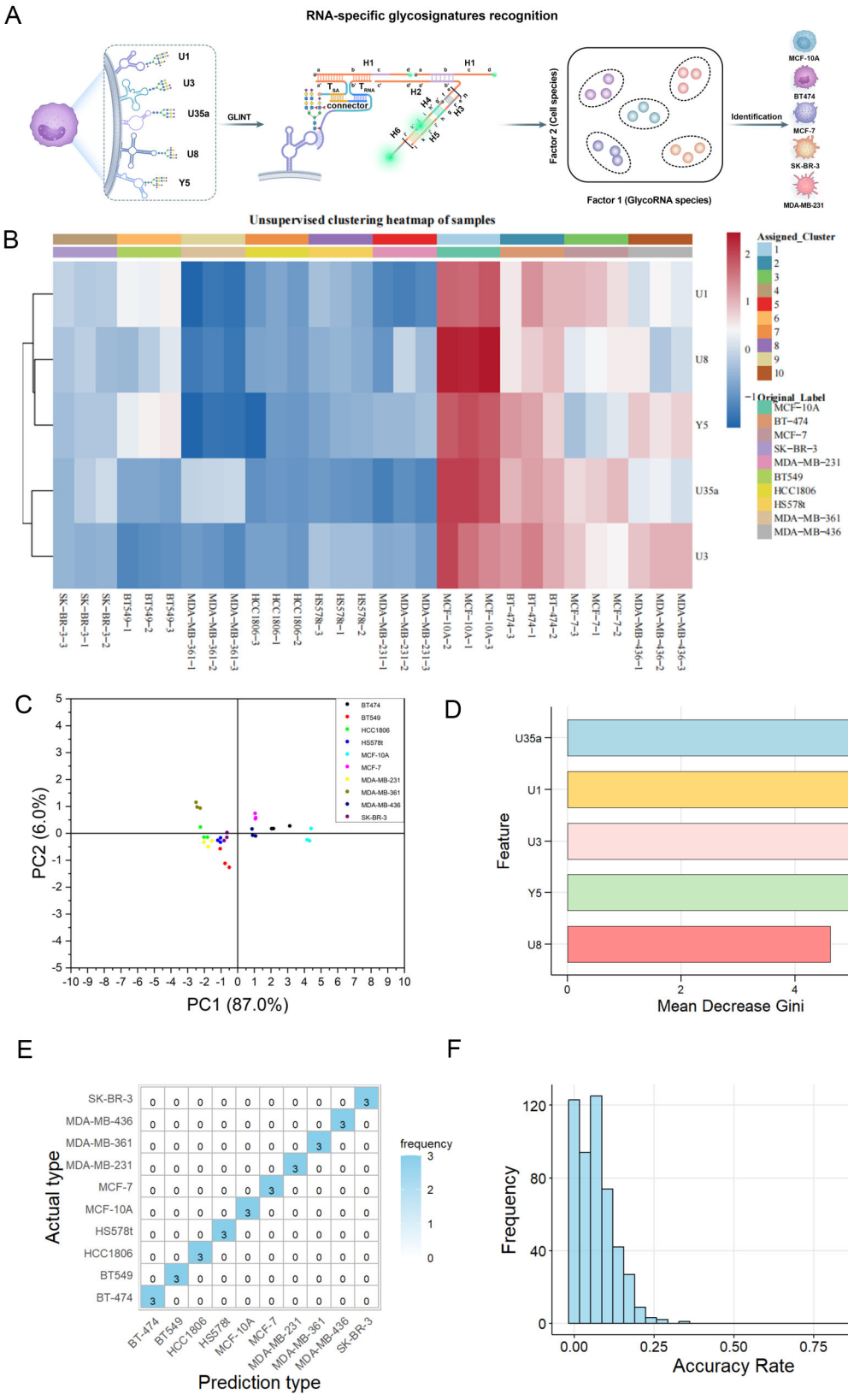

Figure 6. Demonstration of the application of GLINT in the classification of breast cancer subtypes and glycoRNA. (**A**) Schematic illustration of GLINT application in subtyping breast cancer cells. (**B**) Unsupervised hierarchical clustering heatmap of 10 breast cell lines based on the expression profiles of five glycoRNAs. (**C**) Principal component analysis (PCA) discrimination of 10 breast cancer cell subtypes using the GLINT signals from five glycoRNAs. The sample groups were encoded according to the indicated colors. (**D**) Feature importance ranking of five glycoRNAs in breast cancer subtype classification via random forest analysis. (**E**) Confusion matrix of the random forest classification model for 10 breast cell lines based on glycoRNA expression profiles. (**F**) Permutation test results for the random-forest classifier validated by leave-one-out cross-validation (LOOCV).

lighting the excellent classification performance of the model (Fig. 6F).

Together, these results demonstrate that glycoRNA expression exhibits systematic and significant differences across breast cancer subtypes, and that glycoRNA expression profiles enable high-accuracy classification of breast cancer cell line subtypes. These findings further validate that our GLINT assay possesses excellent stability, specificity, and capacity to distinguish breast cancer.

Discussion

In this study, we developed a glycoRNA-lighted *in situ* nanotracking strategy that enables highly reliable *in situ* imaging of cell surface glycoRNAs. By integrating the biological dual-recognition module with a dual hierarchical HCR, the GLINT system effectively minimizes signal leakage and overcomes the limitation of low amplification efficiency associated with hybridization chain reactions. The dual-recognition module improves specificity by independently targeting the glycan and RNA components of glycoRNAs, thereby preventing unintended labeling of glycoproteins or glycolipids and minimizing signal crosstalk, which enables high-precision detection of glycoRNA. Subsequently, concatenated dual hierarchical HCR circuits generate high-molecular-weight hyperbranched DNA nanostructures, and fluorescent group modification of the DNA strands enables efficient amplification of the HCR reaction and substantial signal enhancement. In addition, using GLINT labeling combined with immunofluorescence colocalization and siRNA-mediated knockdown of SNARE proteins, we demonstrated that the intracellular trafficking and plasma membrane localization of glycoRNAs depend on SNARE complex-mediated vesicle secretion and membrane fusion. In addition, we observed that glycoRNAs at the cell surface were primarily enriched in lipid raft domains. These findings are consistent with previous reports that glycoRNA membrane localization relies on classical vesicle trafficking pathways and provide a mechanistic basis for further investigation into the extracellular biological functions of glycoRNAs. Furthermore, we systematically profiled the expression levels of five target glycoRNAs in ten breast cancer cell lines using the GLINT strategy. Principal component analysis, unsupervised hierarchical clustering, and leave-one-out cross-validation (LOOCV) revealed that glycoRNA expression profiles enabled high-accuracy classification of distinct breast cancer subtypes, with a mean classification accuracy of 100%. Moreover, the permutation test demonstrated that the association between glycoRNA expression profiles and breast cancer cell subtypes is statistically significant. These findings suggest that glycoRNA signatures hold promise as molecular biomarkers for breast cancer subtyping and provide a novel framework for expanding the application of glycoRNAs in cancer diagnostic development.

Funding

This work was supported by the National Science and Technology Major Project (2025ZD0551102); the National Natural Science Foundation of China (82372352, 82122042, 82502825, and U23A2047). Funding to pay the Open Access publication charges for this article was provided by the National Natural Science Foundation of China.

Data availability

The data underlying this article are available in the article and in its online supplementary material.

Acknowledgements

Author contributions: M.G. (Data curation [lead], Formal Analysis [lead], Methodology [lead], Software [lead], Writing – original draft [lead], Writing – review & editing [lead]), X.T. (Methodology [equal], Writing – original draft [equal], Writing – review & editing [equal]), Z.X. (Data curation [supporting]), B.N. (Software [supporting], Supervision [supporting]), R.D. (Methodology [supporting], Software [supporting]), W.F. (Formal Analysis [supporting]), Y.Y. (Visualization [supporting]), Y.T. (Data curation [supporting], Resources [supporting]), J.L. (Formal Analysis [supporting], Methodology [supporting]), J.S. (Methodology [supporting]), Y.Z. (Investigation [supporting], Project administration [supporting]), K.C. (Project administration [supporting], Resources [supporting], Writing – original draft [supporting], Writing – review & editing [supporting]).

Supplementary data

Supplementary data is available at NAR online.

Conflict of interest

None declared.

References

1. Flynn RA, Pedram K, Malaker SA *et al.* Small RNAs are modified with N-glycans and displayed on the surface of living cells. *Cell* 2021;184:3109–3124. https://doi.org/10.1016/j.cell.2021.04.023
2. Reily C, Stewart TJ, Renfrow MB *et al.* Glycosylation in health and disease. *Nat Rev Nephrol* 2019;15:346–66. https://doi.org/10.1038/s41581-019-0129-4
3. Zhang N, Tang W, Torres L *et al.* Cell surface RNAs control neutrophil recruitment. *Cell* 2024;187:846–860. https://doi.org/10.1016/j.cell.2023.12.033
4. Liu YS, Miao YL, Dou Y *et al.* Processing of N-glycans in the ER and golgi influences the production of surface sialylated glycoRNA. *Glycoconj J* 2024;41:361–70 https://doi.org/10.1007/s10719-024-10171-w
5. Sharma S, Jiao X, Yang J *et al.* Extracellular exosomal RNAs are glyco-modified. *Nat Cell Biol* 2025;27:983–91. https://doi.org/10.1038/s41556-025-01682-1
6. Ma Y, Guo W, Mou Q *et al.* Spatial imaging of glycoRNA in single cells with ARPLA. *Nat Biotechnol* 2024;42:608–16. https://doi.org/10.1038/s41587-023-01801-z
7. Michael FS, Hamouda MB, Stupak J *et al.* Identification of glycosylated nucleosides in small synthetic glyco-RNAs. *Chem Bio Chem* 2024;25:e202300784. https://doi.org/10.1002/cbic.202300784
8. Robinson PV, de Almeida-Escobedo G, de Groot AE *et al.* Live-cell labeling of specific protein glycoforms by proximity-enhanced bioorthogonal ligation. *J Am Chem Soc* 2015;137:10452–5. https://doi.org/10.1021/jacs.5b04279
9. Xie Y, Chai P, Till NA *et al.* The modified RNA base acp(3)U is an attachment site for N-glycans in glycoRNA. *Cell* 2024;187:5228–5237. https://doi.org/10.1016/j.cell.2024.07.044
10. Guo X, Tariq M, Lai Y *et al.* Capture of the newly transcribed RNA interactome using click chemistry. *Nat Protoc* 2021;16:5193–219. https://doi.org/10.1038/s41596-021-00609-y

11. Li Y, Qian Y, Lei T *et al.* Simple and rapid lectin-based detection of native glycoRNAs. *Biorxiv* 2024;2024:12.09.627596. 2024 09 December 2024, preprint: not peer reviewed.
12. Liu H, Li X, Ren Y *et al.* In situ visualization of RNA-specific sialylation on living cell membranes to explore N-glycosylation sites. *J Am Chem Soc* 2024;146:8780–6. https://doi.org/10.1021/jacs.4c01826
13. Wang H, Wang H, Willner I *et al.* High-performance biosensing based on autonomous enzyme-free DNA circuits. *Top Curr Chem (Z)* 2020;378:20. https://doi.org/10.1007/s41061-020-0284-x
14. Liu J, Zhang Y, Xie H *et al.* Applications of catalytic hairpin assembly reaction in biosensing. *Small* 2019;15:e1902989. https://doi.org/10.1002/smll.201902989
15. Li B, Jiang H, Luo S *et al.* Enzyme-accelerated catalytic DNA circuits enable rapid and one-pot detection of bacterial pathogens. *Biosens Bioelectron* 2025;267:116822. https://doi.org/10.1016/j.bios.2024.116822
16. Wu Q, Xu W, Shang J *et al.* Autocatalytic DNA circuitries. *Chem Soc Rev* 2024;53:10878–99. https://doi.org/10.1039/D4CS00046C
17. Li H, Wang X, Wei S *et al.* Applications of hybridization chain reaction optical detection incorporating nanomaterials: a review. *Anal Chim Acta* 2022;1190:338930. https://doi.org/10.1016/j.aca.2021.338930
18. Bi S, Yue S, Zhang S., Hybridization chain reaction: a versatile molecular tool for biosensing, bioimaging, and biomedicine. *Chem Soc Rev* 2017;46:4281–98. https://doi.org/10.1039/C7CS00055C
19. Wang H, He Y, Wei J *et al.* Construction of an autocatalytic hybridization assembly circuit for amplified in vivo microRNA imaging. *Angew Chem Int Ed* 2022;61:e202115489. https://doi.org/10.1002/anie.202115489
20. Gao Y, Chen Y, Shang J *et al.* Enzyme-free autocatalysis-driven feedback DNA circuits for amplified aptasensing of living cells. *ACS Appl Mater Interfaces* 2022;14:5080–9. https://doi.org/10.1021/acsami.1c22767
21. Xing C, Chen Z, Zhang C *et al.* Target-directed enzyme-free dual-amplification DNA circuit for rapid signal amplification. *J Mater Chem* 2020;8:10770–5.
22. Li R, Zhu Y, Gong X *et al.* Self-stacking autocatalytic molecular circuit with minimal catalytic DNA assembly. *J Am Chem Soc* 2023;145:2999–3007. https://doi.org/10.1021/jacs.2c11504
23. Jiang YS, Bhadra S, Li B *et al.* Mismatches improve the performance of strand-displacement nucleic acid circuits. *Angew Chem Int Ed* 2014;53:1845–8. https://doi.org/10.1002/anie.201307418
24. Wei K, Xu Y, Nie C *et al.* A multifunctional peptide nucleic acid/peptide copolymer-based dual-mode biosensor with macrophage-hitchhiking for enhanced tumor imaging and urinalysis. *J Am Chem Soc* 2024;146:33075–83. https://doi.org/10.1021/jacs.4c10562
25. Jalili R, Horecka J, Swartz JR *et al.* Streamlined circular proximity ligation assay provides high stringency and compatibility with low-affinity antibodies. *Proc Nat Acad Sci USA* 2018;115:E925–E933.
26. Kizer ME, Linhardt RJ, Chandrasekaran AR *et al.* A molecular hero suit for *in vitro* and *in vivo* DNA nanostructures. *Small* 2019;15:e1805386. https://doi.org/10.1002/smll.201805386
27. Ren T, Zhang Y, Tong Y *et al.* FRET imaging of glycoRNA on small extracellular vesicles enabling sensitive cancer diagnostics. *Nat Commun* 2025;16:3391. https://doi.org/10.1038/s41467-025-58490-2
28. Lv WY, Li CH, Li YF *et al.* Hierarchical hybridization chain reaction for amplified signal output and cascade DNA logic circuits. *Anal Chem.* 2021;93:3411–7. https://doi.org/10.1021/acs.analchem.0c04483
29. Li S, Tang Y, Hu L *et al.*. Autonomously driving multiplexed hierarchical hybridization chain reaction of a DNA cobweb sensor for monitoring intracellular microRNA. *Sens Actuators, B* 2021;344:0925–4005. https://doi.org/10.1016/j.snb.2021.130205
30. Liu L, Liu JW, Wu H *et al.* Branched hybridization chain reaction circuit for ultrasensitive localizable imaging of mRNA in living cells. *Anal Chem* 2018;90:1502–5. https://doi.org/10.1021/acs.analchem.7b04848
31. Manders EMM, Verbeek FJ, Aten JA., Measurement of co-localization of objects in dual-colour confocal images. *J Microsc* 1993;169:375–82. https://doi.org/10.1111/j.1365-2818.1993.tb03313.x
32. Sezgin E, Levental I, Mayor S *et al.* The mystery of membrane organization: composition, regulation and roles of lipid rafts. *Nat Rev Mol Cell Biol* 2017;18:361–74. https://doi.org/10.1038/nrm.2017.16

Received: October 20, 2025. **Revised:** April 1, 2026. **Accepted:** April 6, 2026